Geophysical Journal International

Geophys. J. Int. (2023) **233,** 2208–2214
Advance Access publication 2023 February 14
GJI Seismology

https://doi.org/10.1093/gji/ggad061

Source parameter analysis using distributed acoustic sensing – an example with the PoroTomo array

Xiaowei Chen

Texas A&M University, College Station, TX 77845, USA. E-mail: xiaowei.chen@tamu.edu

Accepted 2023 January 27. Received 2023 January 14; in original form 2022 October 28

SUMMARY

In this study, I demonstrate that distributed acoustic sensing (DAS) raw strain rate data can directly be used to estimate spectral source parameters through an Empirical Green's Function (EGF) deconvolution analysis. Previously, DAS had been widely used in passive seismology to image the subsurface and analyze ground motion variations by converting strain or strain rate to particle velocity or acceleration prior to analysis. In this study, spectral analysis is applied to the PoroTomo joint DAS and seismic Nodal array in the Brady Hot Springs geothermal field to obtain source parameters for two M4 earthquakes via EGF analysis, where nearly collocated smaller events are used as an EGF to remove path and site effects. The EGF workflow is applied to raw DAS strain rate data without conversion to particle velocities and raw Nodal seismic data. The DAS and Nodal results are very consistent with similar features of spectral ratios, corner frequencies and moment ratios for the same event pairs. The uncertainty due to stacked spectral measurement is much lower on the DAS array, suggesting better stability of spectral shape measurement, possibly due to the much denser spatial sampling. The uncertainty due to model fitting is similar between DAS and Nodal arrays with slightly lower uncertainty on the DAS array. These observations demonstrate potential for directly using the strain rate measurements from DAS arrays for earthquake source characterizations.

Key words: Distributed Acoustic Sensing; Earthquake source observations; Empirical Green's Function; Seismology.

1. INTRODUCTION

Distributed Acoustic Sensing (DAS) can transform fiber cables into densely spaced seismic sensors and measure strain or strain-rate. This technique has been rapidly growing in the last decade in passive seismology (Zhan 2019; Lindsey & Martin 2021). Previous studies have used DAS data for near-surface velocity structure (Dou *et al.*2017; Ajo-Franklin *et al.*2019) and teleseismic and receiver function analyses (Lindsey *et al.*2017; Yu *et al.*2019). Wang *et al.* (2018) performed detailed analysis of strain-velocity conversion for a M4.3 earthquake using data recorded by the PoroTomo joint DAS/Nodal array in Brady Hot Springs Geothermal field and obtained good agreement between these two arrays, suggesting that DAS could capture the ground motion amplitude variations. Yang *et al.* (2022) obtained high-resolution correlation between shallow velocity (Vs30) and ground motion variations using DAS array, suggesting that DAS is subject to similar site amplifications as seismic stations.

However, relatively fewer studies have explored earthquake source parameters using DAS array. Previous studies usually converted strain or strain-rate to particle velocities prior to data analysis. For example, Yang *et al.* (2022) converted DAS to acceleration prior to measuring site amplifications. Lior *et al.* (2021) converted strain to ground motion before measuring stress drop and magnitude. The requirement for data conversion limits real-time analysis of DAS data for rapid responses, such as earthquake early-warning. Lellouch *et al.* (2020) directly used DAS data to determine microseismic event magnitudes and found good agreement between DAS and geophone arrays at the FORGE geothermal field.

In this study, I apply spectral analysis to the raw DAS data without conversion to particle velocity. An Empirical Green's Function (EGF) workflow is applied to DAS and Nodal arrays separately for two M4 earthquakes located at regional distances of ∼120 and 150 km. EGF analysis has been widely used in earthquake seismology to retrieve earthquake source parameters, where the closely located smaller event is used as an EGF to remove the propagation and site effect from a larger event. Several previous studies used dense seismic arrays to investigate the source processes of small earthquakes and quantifying source parameter uncertainties (e.g. Kane *et al.*2011; Fan & McGuire 2018; Pennington *et al.*2022). In this case, given the large source-receiver distance (>100 km), the small spacing between stations (∼ a few meters) and the small size of the array (∼ 1 km), the entire array is equivalent to a single seismic station and the propagation effect should be very similar within the array, so this array is well suited to study the coherency and consistency of spectra.

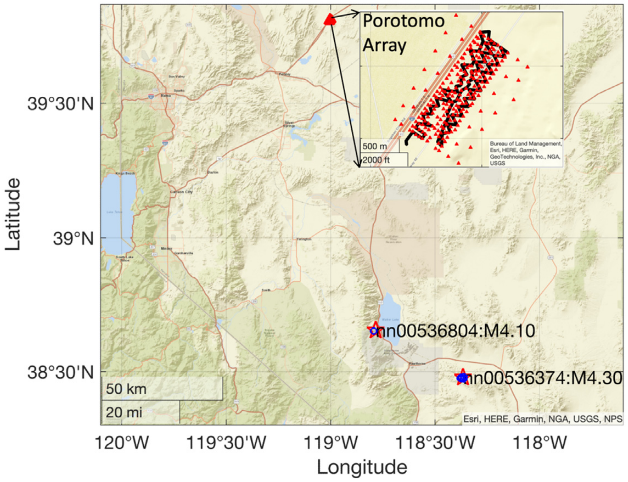

Figure 1. Map view of the study area. The Porotomo Array is shown on the top as red triangles. The inset shows detailed array geometry (red triangles are Nodal stations, black circles are DAS channels). The two target earthquakes are shown as red star and the EGF events are shown as blue circles.

Due to the limited azimuthal coverage, analysis in this study will not resolve detailed source process of the two M4 events, as a single station measurement is insufficient to address rupture directivity or source complexity effects, rather, the primary goals of this study are to investigate whether DAS data can be directly used for spectral analysis and whether the measured source parameters (and their associated uncertainties) are comparable to those from a seismic array. These results will have important implications for future studies that directly use DAS measurements for earthquake source characterization.

2. DATA

The PoroTomo (Poroelastic Tomography) array was deployed in the Brady Hot Springs geothermal field in Nevada during March 2016 (Wang *et al.*2018). The array is approximately 1500 m (length) by 500 m (width), consisting of collocated DAS channels and Nodal (Fairfield Zland 3C) stations (Fig. 1). The 242 Nodal stations are buried at a depth of about 0.3 m and record at 500 Hz sampling rates. These sensors have a natural frequency of 5 Hz. The DAS array utilizes fiber cable approximately 8700 meters long, has a gauge length of 10 m and channel spacing of 1 m (total 8622 channels). The strain-rate is measured at 1000 Hz sampling rate on the DAS array (Wang *et al.*2018).

Wang *et al.* (2018) analyzed the ground motion of a M4.3 earthquake located at 150 km distance from the PoroTomo array, which has high signal to noise ratio. In this study, I search for regional earthquakes within 200 km that are larger than magnitude 4 and potential EGF events larger than M2.5 that are within 2 km (epicentral distance) of the M4 events: target #1-nn00536804–M4.1 (120 km away) and target #2-nn00536374–M4.3 (150 km away), the latter is the one analyzed in Wang *et al.* (2018) (Fig. 1 and Table 1). For target #1, only one EGF event is found. For target #2, six potential EGF events are found. Therefore, total of nine earthquakes are included in the analysis (two target events and seven EGF events).

For each earthquake, I extract waveform starting 5 s before roughly estimated P-wave arrivals and 50 s after S-wave arrivals. These P- and S-wave arrivals are based on averaged source-receiver distance and constant Vp of 5.5 km s^{-1} and Vs of 3 km s^{-1}. Then I manually pick P and S arrivals based on the wavefield image and stacked traces. Given the source-receiver distance and the array geometry, the travel time variations within the array are mostly within 0.5 s, so I use common arrival times for all DAS channels and all nodal stations for each event (see wavefield for the two target events in Fig. 2 and Fig. S1 for all EGFs). Note that because of some timing errors for the DAS array, the arrival times between DAS and Nodal arrays are not the same.

Next, I calculate P-wave spectra using a 2-s window after the P-wave arrival, S-wave spectra using 8-s window after the S-wave arrival and noise-spectra using 2-s window before the P-wave arrival. For the Nodal arrays, the P-wave and P-wave noise spectra are calculated from vertical components and the S-wave and S-wave noise spectra are calculated from the geometrical mean of the two horizontal channels. I test three algorithms to calculate spectra: pmtm (multi-taper) and pwelch (Welch method) from MATLAB and the multitaper algorithm developed by Prieto *et al.* (2009). While the two multitaper algorithms resulted in highly similar spectra (both with time-bandwidth of 6 and 11 tapers), spectra from pwelch tend to have inconsistencies (see example in Fig. S2). The following analysis is focused on S-wave spectra from pmtm algorithm and 8-s time window.

3. EGF ANALYSIS

The recorded waveform is a convolution of event source term, propagation term and site term. A smaller event that is nearly collocated to the larger event can be used as EGF to remove propagation and site terms from the larger event. This method has been used in many different studies to analyze source properties (e.g. Abercrombie 2015; Huang *et al.*2017; Wu *et al.*2019). Visual inspection suggests that some EGF events have low signal-to-noise (SNR) ratio (Fig. S1). EGF 2–4 seems to coincide with a local active-source (sweep) signal, causing a different waveform patterns than the other events (Figs S1d and h). I apply an automated selection and quality control process and do not remove these low SNR events prior to analysis. I follow these processing steps for S-waves from DAS and Nodal arrays:

(1) For each target-EGF pair, calculate the spectral ratio at each frequency point for which both target and EGF events have SNR higher than 2. Only individual spectral ratios that have SNR higher than 2 for all frequency points between 0.5 and 15 Hz (used for spectral fitting) are retained and used to calculate an average spectral ratio. Pairs with less than 40 individual spectral ratios are removed. The numbers of spectral ratios that passed the SNR requirement for each pair is listed in Table 1 and EGF 2–3 (M2.5) is removed due to insufficient number of stations that passed the SNR criteria. An example of the SNR and spectral ratio is shown in Fig. 3 with EGF 2–5 for target #2. Waveform similarity for DAS channels and Nodal stations that passed the SNR criterion is also obtained with bandpass filter of 1–6 Hz (Table 1 and Fig. S3), which is used to evaluate EGF selections and qualities.

(2) Use a non-linear optimization solver in MATLAB to find the best-fitting f_c, f_{c2} and moment ratio (M_o) based on the Brune source model (Brune 1970),

$$SR\ (f) = M_o \frac{1 + \left(\frac{f}{f_{c2}}\right)^2}{1 + \left(\frac{f}{f_c}\right)^2}, \qquad (1)$$

Table 1. List of events included in the analysis. The values in 'CC' column represent averaged CC for Nodal and DAS arrays, respectively. The values in 'Nspec' column represent number of individual spectral ratios for stacking from Nodal and DAS arrays, respectively. Rows with purple color and bold font denote target events, rows with grey color denote EGF did not pass the quality check, row with blue color denote the EGF event that has highest CC value and shown as example in Fig. 3. There are 242 Nodal stations and 8622 DAS channels available in the data set.

Time (UTC)	Latitude	Longitude	Dep (km)	Ml	id	Note	CC (Nodal, DAS)	Nspec (Nodal, DAS)
2016–03-22T12:35:34.048Z	38.653	– 118.7938	8.8	2.8	nn00536848	EGF 1–1	0.22,0.22	114, 664
2016–03-22T10:00:45.356Z	**38.6555**	**– 118.7841**	**10.9**	**4.1**	**nn00536804**	**Target#1**	–	–
2016–03-25T06:20:52.238Z	38.4754	– 118.3747	7.6	2.5	nn00537532	EGF 2–1	0.53,0.50	167, 2093
2016–03-23T20:10:39.905Z	38.481	– 118.3622	6.2	3.4	nn00537228	EGF 2–2	0.53,0.55	169, 2620
2016–03-22T13:44:13.223Z	38.4758	– 118.3792	5.4	2.5	nn00536856	EGF 2–3	–	–
2016–03-21T23:31:27.004Z	38.4742	– 118.3745	3.7	3	nn00536692	EGF 2–4	0.58,0.56	131, 185
2016–03-21T13:18:09.767Z	38.4741	– 118.363	4.5	3.4	nn00536452	EGF 2–5	0.81,0.76	112, 3797
2016–03-21T10:46:49.914Z	38.479	– 118.3746	5.8	3.3	nn00536423	EGF 2–6	0.55,0.51	123, 3850
2016–03-21T07:37:10.535Z	**38.4792**	**– 118.3662**	**9.9**	**4.3**	**nn00536374**	**Target#2**	–	–

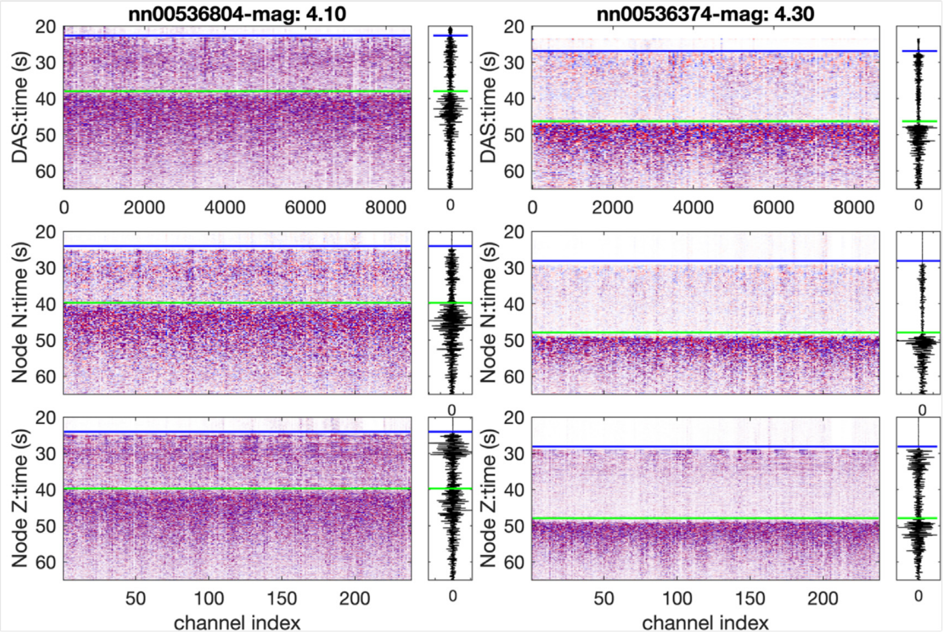

Figure 2. Wavefield for the two target earthquakes. Top: DAS and stacked DAS, middle: Nodal N-component and stacked Nodal N, bottom: Nodal-Z component and stacked Nodal Z. Blue line is manually picked P arrival. Green line is manually picked S arrival.

where f_c and f_{c2} are the corner frequencies for the target and EGF events, respectively.

(3) Calculate the misfit between observation and best-fitting model, then calculate variance reduction following Uchide & Imanishi (2016),

$$\text{residual} \; = \log_{10} SR^{obs}(f) \; - \log_{10} SR^{syn}(f; M_o, f_c, f_{c2}) \qquad (2)$$

$$Vr \; = 1 - \frac{\sum (\text{residual})^2}{\sum (SR^{\text{obs}} - \text{mean}\,(SR^{\text{obs}}))^2} \qquad (3)$$

Only pairs with variance reduction larger than 0.8 are saved. All remaining pairs passed the variance reduction criterion, including the EGF that coincided with active source. The misfit is used to calculate a peak-to-peak ratio of the deviation from Brune source model, which represents some degree of source complexity. Uchide & Imanishi (2016) calculated the peak-to-peak ratio as a single value for the entire frequency range. The modified version from Pennington *et al.* (2023) that calculates the ratio as a function of frequency is used here (Fig. 3 and Figs S4–S7). Since the PoroTomo array has very limited azimuthal coverage for the target events, the complexity is not further discussed in this study.

(4) Quantify source parameter uncertainties using two methods. The first method examines the intra-array variability and the stability of the stacked spectral ratio and the uncertainty is referred to as 'Err-array'. Err-array is obtained via 100 bootstrap resamples, each resample randomly select 25 per cent of individual spectral ratios that passed SNR requirement. The Err-array for each parameter is set as the 90th confidence interval from the bootstrap resamples. The second method examines uncertainty due to model fitting and the uncertainty is referred to as 'Err-fit'. Err-fit is obtained following Yoshimitsu *et al.* (2019) via bootstrap resamples of the residual between best-fitting model and observation. For each resample, randomly selected values from the residual are added to the best-fitting spectral ratio model, then a new set of parameters (M_o, f_c and f_{c2}) are obtained. The Err-fit is set as the 90th confidence interval from bootstrap resamples. Yoshimitsu *et al.* (2019) rejected pairs with M_o uncertainty exceeds 100, f_c and f_{c2} uncertainties exceed 1.5 Hz.

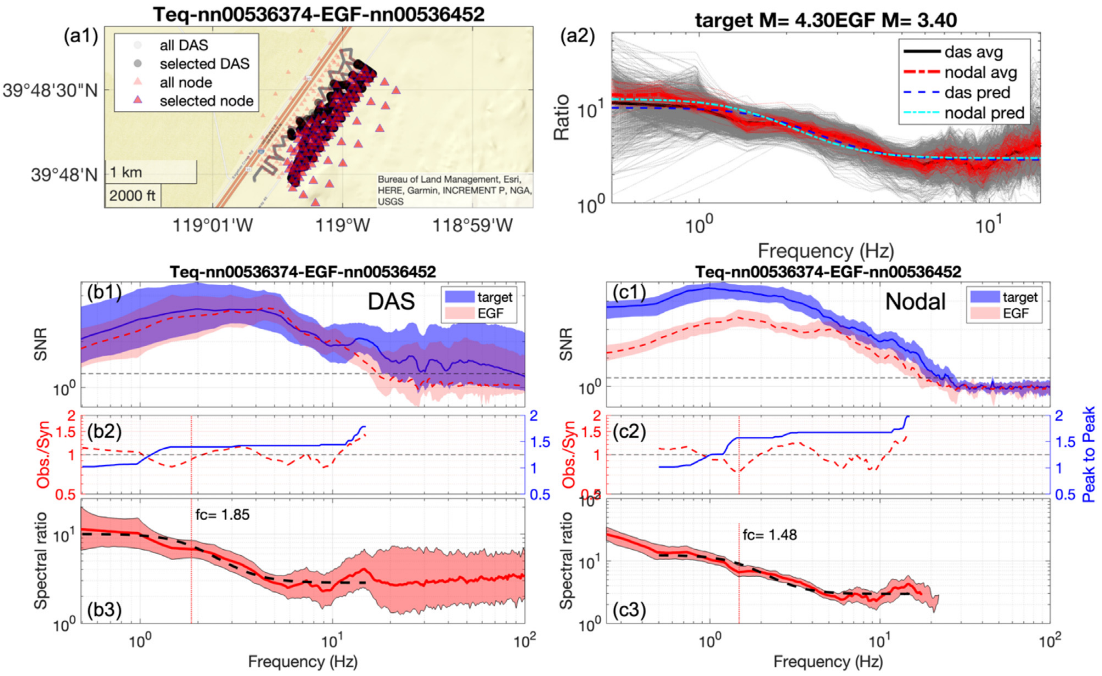

Figure 3. Example analysis for EGF 2–5 and target #2. (a1) Map view of all DAS channels (light grey circles) and Nodal stations (light red triangles) and those that passed SNR requirement (large grey circles and large red triangles). (a2) Individual spectral ratio for DAS (thin grey lines) and Nodal (thin red lines), averaged spectral ratio (thick black solid and red dash lines) and best-fitting models (dashed blue and cyan lines). (b1)–(b3) and (c1)–(c3) are results for DAS and Nodal arrays, respectively. (b1) and (c1) are SNR – solid blue and red dash lines are averaged SNR and the shading area represents 90 per cent confidence limit at each frequency point. (b2) and (c2) are residual from best-fitting model (red dash line) and peak-to-peak ratio of the deviation (blue solid line). (b3) and (c3) are observed spectral ratio (thick solid red line) and the 90 per cent confidence limit (light red shading) and best-fitting model (thick black dash line). The red dashed vertical lines in (b2), (b3), (c2) and (c3) denote the best-fitting corner frequency for the target earthquake.

4. RESULTS AND DISCUSSION

Out of the seven available target-EGF pairs, EGF 2–3 is removed due to low SNR, EGF 2–4 (waveform compromised by active source) is rejected due to unconstrained f_{c2} (uncertainty exceeds 10 000 Hz). The other five pairs passed the automated workflow and their results are summarized in Table 2 and Fig. 4. These results show that:

(1) For individual event pairs, the shape of the spectral ratio (see Figs 3 and S3–S6, the locations of holes and bumps agree well) and the measured source parameters (Fig. 4) are very consistent between DAS and Nodal arrays. Although corner frequencies (f_c and f_{c2}) from DAS arrays are slightly higher than Nodal array, the differences are mostly within 5 per cent, typically less than measurement uncertainty; the moment ratio (M_o) has slightly higher variation, but still within 15 per cent.

For a plane wave propagating in x-direction, the strain can be related to particle velocity via: $\epsilon = \frac{\partial u}{\partial x} = \frac{1}{c}\frac{\partial u}{\partial t} = \frac{v}{c}$ (Wang *et al.*2018), where $1/c$ is the apparent slowness and v is the ground velocity. Many methods have been proposed to convert strain to velocity (or strain rate to acceleration) (e.g. Wang *et al.*2018; Yang *et al.*2022). For the M4.3 event, Wang *et al.* (2018) used multiple methods to compare DAS and Nodal waveforms and found different methods produce slightly different results and the converted waveforms are similar but do not always agree exactly. By taking ratio in frequency domain between two events at the same station, the common constants (slowness) and common propagation/site effects cancel out, so the resulted spectral ratio should be similar between DAS channel and Nodal stations. The observed agreement in source parameters confirms that DAS can be directly used for source parameter analysis.

(2) Although the SNR of individual DAS channels is typically lower than Nodal stations, the locations of the DAS channels and Nodal stations that passed the SNR requirement are mostly consistent, which is similar to the SNR spatial patterns for the M4.3 earthquake observed in Wang *et al.* (2018). It is interesting to note that the SNR on the Nodal array drops below 2 beyond 20 Hz for both target and EGF events in Fig. 3, but some DAS channels seem to have high SNR even at higher frequency. This could potentially expand the usable bandwidth for future applications.

(3) The Err-array is much smaller than Err-fit for all three parameters (Fig. 4 middle and bottom rows), suggesting that dense arrays provide stable measurement of spectral ratios, but complexities in spectral ratio may cause larger values for Err-fit. For f_c and f_{c2}, Err-array from DAS is typically much smaller than the Nodal array, likely due to the dense spatial sampling from the DAS array, as the number of usable DAS channels is much larger than usable Nodal stations (Table 1). Err-fit is similar between DAS and Nodal arrays, with slightly lower uncertainty from DAS array. The similar Err-fit suggests that features in spectral ratio (such as bumps or holes) are captured by both DAS and Nodal arrays (e.g. see Fig. 3).

(4) Trade-off between source parameters is examined in Fig. 4 top row. Strong tradeoff exists between f_c and f_{c2}: when f_c from DAS array is higher than Nodal array, f_{c2} is also higher. Tradeoff between frequency-dependent parameters is consistent with previous studies (e.g. Shearer *et al.*2019; Chen & Abercrombie 2020). No clear tradeoff is observed between corner frequencies and M_o.

(5) The variability of the target event corner frequency between different EGF events is much larger than the uncertainties from individual event pairs. Yoshimitsu *et al.* (2019) established three criteria to reject EGF pairs and found that individual measurements after

Table 2. Summary of source parameters from the five EGF pairs. For M_o, f_c and f_{c2}, the three values represent: source parameter value (bold font), Err-array (uncertainty from resampling spectral ratio), Err-fit (uncertainty from resampling residual). Event 2–5 is shown in Fig. 3.

EGF	Nodal									DAS								
	M_o(ratio)			f_c(Hz)			f_{c2}(Hz)			M_o(ratio)			f_c(Hz)			f_{c2}(Hz)		
1–1	**85.9**	9.5	6.9	**2.33**	0.24	0.2	**7.15**	0.63	0.82	**96.9**	9.1	7.6	**2.39**	0.16	0.2	**7.46**	0.34	0.71
2–1	**55.4**	4.6	5.9	**2.33**	0.22	0.24	**7.53**	0.75	1.21	**59.8**	2.9	5.4	**2.36**	0.11	0.23	**7.52**	0.35	0.98
2–2	**12.8**	1	1.6	**1.97**	0.13	0.26	**6.11**	0.34	0.93	**11.3**	0.4	1.4	**2.16**	0.05	0.29	**6.23**	0.18	0.93
2–5	**12.4**	1.1	1	**1.48**	0.17	0.15	**3.03**	0.33	0.27	**10**	0.2	0.5	**1.85**	0.05	0.15	**3.46**	0.09	0.27
2–6	**13.1**	0.5	0.7	**3.59**	0.43	0.41	**6.85**	1.01	0.96	**12.9**	0.2	0.9	**3.68**	0.14	0.39	**7.04**	0.31	0.88

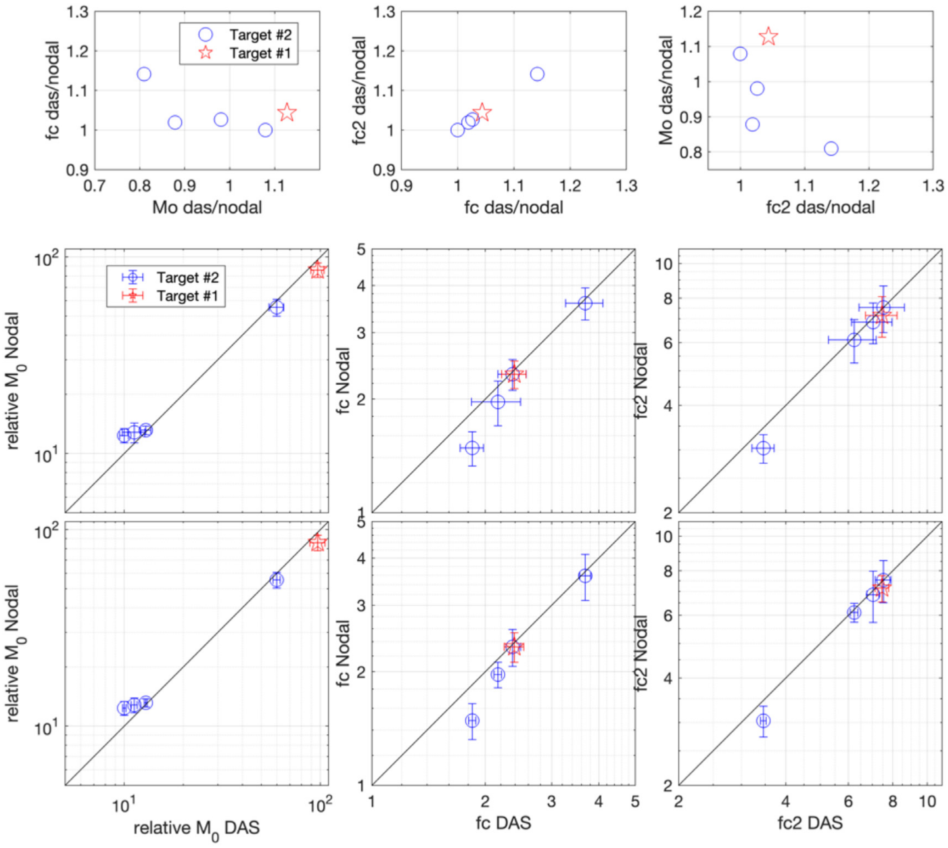

Figure 4. Comparison of parameter inversion using DAS and Nodal arrays. For all figures, blue circles denote parameters for Target #2 and red star denotes parameters for Target #1. Top row: Parameter ratio between DAS and Nodal array to check potential trade-off between parameters. Middle row: Uncertainties from model fitting (randomly resample residuals, 'Err-fit'). Bottom row: Uncertainties from array stacking (randomly resample individual spectral rations within the array, 'Err-array'). The 'relative M$_0$' refers to 'relative moment for each pair between target and EGF event'.

selection are more consistent. Pennington *et al.* (2022) found that the EGF event with the lowest focal mechanism deviation from the target event resulted with the highest peak slip. However, the focal mechanism solutions are unavailable for the EGF events analyzed here. Some studies use waveform cross-correlation to select EGF. Kane *et al.* (2013) found that CC limit of 0.5 and distance separation of 2 km are ideal for selecting EGFs. Abercrombie (2015) found more consistent spectral ratio and STFs for small earthquakes when using EGF with higher CC cutoff. Out of the 4 EGF events of target #2, the EGF with highest average CC (0.81 for Nodal and 0.76 for DAS with band pass filter of 1–6 Hz) has lowest Err-array and Err-fit and lowest f_c estimation from both DAS and Nodal arrays (Table 2 and Figs 3 and 4), At regional distance, higher CC suggests more consistent path effects between target and EGF events and the lower uncertainties for EGF 2–5 tend to be consistent with expectations based on previous studies.

5. CONCLUSION

Comparison of EGF spectral ratio analyses of two M4 earthquakes using the joint DAS/Nodal array finds strong agreement of source parameters for individual event pairs, include moment ratio, corner frequencies of target and EGF events. Compared to Nodal array, measurements from DAS array have lower 'Err-array' (uncertainties from array stacking) for corner frequencies, implying the stacked spectral ratio is more stable when a subset of channels is used. This is likely due to much dense spatial sampling, as the number of individual spectral ratios used for stacking is much larger from the DAS array. The spectral features are consistent between DAS and Nodal arrays. The uncertainty due to model fitting ('Err-fit') is similar between the two, with slightly lower uncertainty for DAS array. The choice of EGF events affects the source parameter inversion for the M4.3 earthquake for both Nodal and DAS arrays and the EGF (2–5) with highest similarity to the target event yields the lowest overall uncertainty. Overall, these results demonstrate the potential of directly using strain data measured on DAS array for earthquake source characterization via spectral analysis. Some DAS channels appear to have higher SNR than Nodal array for these regional earthquakes at higher frequencies (e.g. > 20 Hz), which may potentially expand usable bandwidth for future applications.

ACKNOWLEDGMENTS

This research is supported by NSF award 2033376. This research is benefited from the IRIS DAS workshop led by Nate Lindsey and Eileen Martin in 2020, where detailed hands-on tutorials on accessing and visualizing data from the PoroTomo array were presented. Comments from editor Jörg Renner, reviewer Annamarie Baltay and an anonymous reviewer significantly improved the manuscript.

SUPPORTING INFORMATION

Supplementary data are available at *GJI* online.

Figure S1. Wavefield for all EGF events (a)–(g). Top: DAS and stacked DAS, middle: Nodal N-component and stacked Nodal N, bottom: Nodal-Z component and stacked Nodal Z. Blue line is manually picked P arrival. Green line is manually picked S arrival. (h): example spectrogram of Nodal station N060 for event nn00536692 (d) that coincides with sweep signal.

Figure S2. Example spectral calculation test with three different methods using the same input data – North component of channel N001 from the Nodal array for the M4.3 event. Both ‘pmtm’ and ‘mtspec’ use time-bandwidth of 6 and 11 tapers.

Figure S3 Waveform correlation between Target and EGF event. For each pair, the left-hand panel shows the correlation at each DAS channel and Nodal station that passed the SNR selection. The right-hand panel shows the stacked CC from the whole array. The target and EGF event ids from Table 1 are shown in the title.

Figure S4. Result for EGF 1-1 and target #1. (a1) Map view of all DAS channels (light grey circles) and Nodal stations (light red triangles) and those that passed SNR requirement (large grey circles and large red triangles). (a2) Individual spectral ratio for DAS (thin grey lines) and Nodal (thin red lines), averaged spectral ratio (thick black solid and red dash lines) and best-fitting models (dashed blue and cyan lines). (b1)–(b3) and (c1)–(c3) are results for DAS and Nodal arrays, respectively. (b1) and (c1) are SNR – solid blue and red dash lines are averaged SNR and the shading area represents 90 per cent confidence limit at each frequency point. (b2) and (c2) are residual from best-fitting model (red dash line) and peak-to-peak ratio of the deviation (blue solid line). (b3) and (c3) are observed spectral ratio (thick solid red line) and the 90 per cent confidence limit (light red shading) and best-fitting model (thick black dash line). The red dashed vertical lines in (b2), (b3), (c2) and (c3) denote the best-fitting corner frequency for the target earthquake.

Figure S5. Result for EGF 2-1 and target #2. (a1) Map view of all DAS channels (light grey circles) and Nodal stations (light red triangles) and those that passed SNR requirement (large grey circles and large red triangles). (a2) Individual spectral ratio for DAS (thin grey lines) and Nodal (thin red lines), averaged spectral ratio (thick black solid and red dash lines) and best-fitting models (dashed blue and cyan lines). (b1)–(b3) and (c1)–(c3) are results for DAS and Nodal arrays, respectively. (b1) and (c1) are SNR – solid blue and red dash lines are averaged SNR and the shading area represents 90 per cent confidence limit at each frequency point. (b2) and (c2) are residual from best-fitting model (red dash line) and peak-to-peak ratio of the deviation (blue solid line). (b3) and (c3) are observed spectral ratio (thick solid red line) and the 90 per cent confidence limit (light red shading) and best-fitting model (thick black dash line). The red dashed vertical lines in (b2), (b3), (c2) and (c3) denote the best-fitting corner frequency for the target earthquake.

Figure S6. Result for EGF 2-2 and target #2. (a1) Map view of all DAS channels (light grey circles) and Nodal stations (light red triangles) and those that passed SNR requirement (large grey circles and large red triangles). (a2) Individual spectral ratio for DAS (thin grey lines) and Nodal (thin red lines), averaged spectral ratio (thick black solid and red dash lines) and best-fitting models (dashed blue and cyan lines). (b1)–(b3) and (c1)–(c3) are results for DAS and Nodal arrays, respectively. (b1) and (c1) are SNR – solid blue and red dash lines are averaged SNR and the shading area represents 90 per cent confidence limit at each frequency point. (b2) and (c2) are residual from best-fitting model (red dash line) and peak-to-peak ratio of the deviation (blue solid line). (b3) and (c3) are observed spectral ratio (thick solid red line) and the 90 per cent confidence limit (light red shading) and best-fitting model (thick black dash line). The red dashed vertical lines in (b2), (b3), (c2) and (c3) denote the best-fitting corner frequency for the target earthquake.

Figure S7. Result for EGF 2-6 and target #2. (a1) Map view of all DAS channels (light grey circles) and Nodal stations (light red triangles) and those that passed SNR requirement (large grey circles and large red triangles). (a2) Individual spectral ratio for DAS (thin grey lines) and Nodal (thin red lines), averaged spectral ratio (thick black solid and red dash lines) and best-fitting models (dashed blue and cyan lines). (b1)–(b3) and (c1)–(c3) are results for DAS and Nodal arrays, respectively. (b1) and (c1) are SNR – solid blue and red dash lines are averaged SNR and the shading area represents 90 per cent confidence limit at each frequency point. (b2) and (c2) are residual from best-fitting model (red dash line) and peak-to-peak ratio of the deviation (blue solid line). (b3) and (c3) are observed spectral ratio (thick solid red line) and the 90 per cent confidence limit (light red shading) and best-fitting model (thick black dash line). The red dashed vertical lines in (b2), (b3), (c2) and (c3) denote the best-fitting corner frequency for the target earthquake.

DATA AVAILABILITY

The earthquake catalog is obtained from USGS earthquake website: https://earthquake.usgs.gov/ and the waveform data is downloaded from DOE website: https://data.openei.org/submissions/3653. The analysis used GISMO package for MATLAB (Reyes & West 2011) and signal processing and optimization toolboxes from MATLAB R2022a.

CONFLICT OF INTEREST

The author declares no financial interest in the subject matter discussed in this manuscript.

REFERENCES

Abercrombie, R. E., 2015. Investigating uncertainties in empirical Green’s function analysis of earthquake source parameters, *J. geophys. Res.,* **120,** 1–15.

Ajo-Franklin, J. B. *et al.*, 2019. Distributed acoustic sensing using dark Fiber for near-surface characterization and broadband seismic event detection, *Sci. Rep.,* **9**(1), 1–14.

Brune, J. N., 1970. Tectonic stress and the spectra of seismic shear waves from earthquakes, *J. geophys. Res.,* **75**(26),.

Chen, X. & Abercrombie, R. E., 2020. Improved approach for stress drop estimation and its application to an induced earthquake sequence in Oklahoma, *Geophys. J. Int.,* **223,** 233–253.

Dou, S. *et al.*, 2017. Distributed acoustic sensing for seismic monitoring of the near surface: a traffic-noise interferometry case study, *Sci. Rep.,* **7**(1), 1–12.

Fan, W. & McGuire, J. J., 2018. Investigating microearthquake finite source attributes with IRIS Community Wavefield Demonstration Experiment in Oklahoma, *Geophys. J. Int.,* **214**(2), 1072–1087.

Huang, Y., Ellsworth, W. L. & Beroza, G. C., 2017. Stress drops of induced and tectonic earthquakes in the central United States are indistinguishable, *Sci. Adv.,* **3**(8), 1–8.

Kane, D. L., Prieto, G. A., Vernon, F. L. & SHearer, P. M., 2011. Quantifying seismic source parameter uncertainties, *Bull. seism. Soc. Am.,* **101**(2), 535–543.

Kane, D. L., Kilb, D. L. & Vernon, F. L., 2013. Selecting empirical Green's functions in regions of Fault complexity: a study of data from the San Jacinto Fault Zone, Southern California, *Bull. seism. Soc. Am.,* **103**(2A), 641–650.

Lellouch, A., Lindsey, N. J., Ellsworth, W. L. & Biondi, B. L., 2020. Comparison between distributed acoustic sensing and geophones: downhole microseismic monitoring of the FORGE geothermal experiment, *Seismol. Res. Lett.,* **91**(6), 3256–3268.

Lindsey, N. J. & Martin, E. R., 2021. Fiber-optic seismology, *Annual Review of Earth and Planetary Sciences,* **49,** 309–336.

Lindsey, N. J., Martin, E. R., Dreger, D. S., Freifeld, B., Cole, S., James, S. R., Biondi, B. L. & Ajo-Franklin, J. B., 2017. Fiber-optic network observations of earthquake wavefields, *Geophys. Res. Lett.,* **44**(23), 11,792–711,799.

Lior, I., Sladen, A., Mercerat, D., Ampuero, J.-P., Rivet, D. & Sambolian, S., 2021. Strain to ground motion conversion of DAS data for earthquake magnitude and stress drop determination, *Solid Earth*. **12,** 1421–1442.

Pennington, C. N., Chang, H., Rubinstein, J. L., Abercrombie, R. E., Nakata, N., Uchide, T. & Cochran, E. S., 2022. Quantifying the sensitivity of microearthquake slip inversions to station distribution using a dense nodal array, *Bull. seism. Soc. Am.,* **112,** 1252–1270.

Pennington, C. N., Wu, Q., Chen, X. & Abercrombie, R. E., 2023 Quantifying rupture characteristics of microearthquakes in the Parkfield area using a high-resolution borehole network, *Geophys. J. Int.*

Prieto, G. A., Parker, R. L. & Vernon, F. L., 2009. A Fortran 90 library for multitaper spectrum analysis, *Comput. Geosci.,* **35**(8), 1701–1710.

Reyes, S. D. & West, M. E., 2011. The Waveform Suite: a robust platform for manipulating waveforms in MATLAB, *Seism. Res. Lett.,* **82**(1), 104.

Shearer, P. M., Abercrombie, R. E., Trugman, D. T. & Wang, W., 2019. Comparing EGF methods for estimating corner frequency and stress drop from P-wave spectra, *J. Geophys. Res.,* **124,** 3966–3986.

Uchide, T. & Imanishi, K., 2016. Small earthquakes deviate from the omega-square model as revealed by multiple spectral ratio analysis, *Bull. seism. Soc. Am.,* **106**(3), 1357–1363.

Wang, H. F., Zeng, X., Miller, D. E., Fratta, D., Feigl, K. L., Thurber, C. H. & Mellors, R. J., 2018. Ground motion response to an ML 4.3 earthquake using co-located distributed acoustic sensing and seismometer arrays, *Geophys. J. Int.,* **213**(3), 2020–2036.

Wu, Q., Chen, X. & Abercrombie, R. E., 2019. Characterizing earthquake source complexity in the trifurcation area of the San Jacinto fault zone, *Presentation at 2019 SCEC Annual Meeting*.

Yang, Y., Atterholt, J. W., Shen, Z., Muir, J. B., Williams, E. F. & Zhan, Z., 2022. Sub-kilometer correlation between near-surface structure and ground motion measured with distributed acoustic sensing, *Geophys. Res. Lett.,* **49**.

Yoshimitsu, N., Ellsworth, W. L. & Beroza, G. C., 2019. Robust stress drop estimates of potentially induced earthquakes in Oklahoma: evaluation of empirical Green's function, *J. Geophys. Res.: Solid Earth,* **124,** 2019JB017483.

Yu, C., Zhan, Z., Lindsey, N. J., Ajo-Franklin, J. B. & Robertson, M., 2019. The potential of DAS in Teleseismic studies: insights from the Goldstone experiment, *Geophys. Res. Lett.,* **46**(3), 1320–1328.

Zhan, Z., 2019. Distributed acoustic sensing turns Fiber-optic cables into sensitive seismic antennas, *Seismol. Res. Lett.,* **91**(1), 1–15.